Hydrophilic Molybdenum Oxide Nanomaterials with Controlled Morphology and Strong Plasmonic Absorption for Photothermal Ablation of Cancer Cells

Guosheng Song,[†,§] Jia Shen,[‡,§] Feiran Jiang,[†] Ronggui Hu,*[,‡] Wenyao Li,[†] Lei An,[†] Rujia Zou,*[,†] Zhigang Chen,[†] Zongyi Qin,[†] and Junqing Hu*[,†]

[†]State Key Laboratory for Modification of Chemical Fibers and Polymer Materials, College of Materials Science and Engineering, Donghua University, Shanghai 201620, China

[‡]State Key Laboratory of Molecular Biology, Institute Biochemistry & Cell Biology, Shanghai Institutes for Biological Sciences, Chinese Academy of Sciences, Shanghai 200031, China

S Supporting Information

ABSTRACT: The molybdenum oxide nanosheets have shown strong localized surface plasmon resonance (LSPR) absorption in the near-infrared (NIR) region. However, the long alky chains of ligands made them hydrophobic and less biocompatible. To meet the requirements of molybdenum based nanomaterials for use as a future photothermal therapy, a simple hydrothermal route has been developed for hydrophilic molybdenum oxide nanospheres and nanoribbons using a molybdenum precursor and poly(ethylene glycol) (PEG). First, molybdenum oxide nanomaterials prepared in the presence of PEG exhibit strong localized surface plasmon resonance (LSPR) absorption in near-infrared (NIR) region, compared with that of no PEG. Second, elevation of synthetic temperature leads to a gradual transformation of molybdenum oxide nanospheres into nanoribbons, entailing the evolution of an intense LSPR absorption in the NIR region. Third, as-prepared molybdenum oxide nanomaterials coated with PEG possess a hydrophilic property and thus can be directly used for biological applications without additional post treatments. Moreover, molybdenum oxide nanoribbons as a model of photothermal materials can efficiently convert the 980 nm wavelength laser energy into heat energy, and this localized hyperthermia produces the effective thermal ablation of cancer cells, meaning a potential photothermal material.

KEYWORDS: Molybdenum oxide, localized surface plasmon resonance, photothermal, morphology-controlled
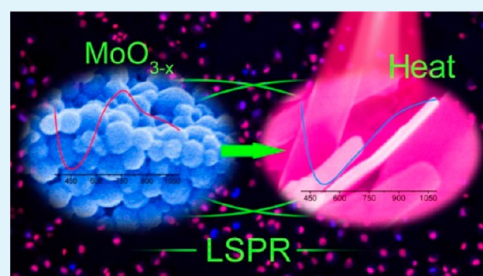
INTRODUCTION

Near-infrared (NIR) laser-induced photothermal ablation (PTA) therapy has attracted much attention in recent years as a promising alternative or supplement to traditional cancer therapies.[1−8] Currently, due to the localized surface plasmon resonance (LSPR), noble metals nanomaterials including Au nanorods,[6,7,9,10] Au nanocages,[11] Au nanoshells,[12,13] and Pd nanosheets[8,14] show strong NIR absorption and have been most widely explored as photothermal agents for cancer treatments.[6−15] However, their practical applications are limited by the high cost of noble metal based nanomaterials.[16,17]

Encouragingly, LSPR is not limited to nanostructures of noble metals and can also be achieved in semiconductor nanocrystals with appreciable free carrier concentration.[16] For example, copper chalcogenide ($Cu_{2−x}S$,[18,19] $Cu_{2−x}Se$,[20,21] and $Cu_{2−x}Te$[18,22]) and transition metal oxides ($WO_{3−x}$[23]), doped semiconductors (tin-doped indium oxide[24] and aluminum-doped zinc oxide[25]) display strong and tunable LSPR, by varying the copper stoichiometric ratio, oxygen deficiency or doped ion of content. On the basis of these, semiconductor nanomaterials have been extensively developed for PTA therapy. As a new type of NIR laser-induced photothermal

agents, these semiconductor nanomaterials such as CuS superstructures,[26] Cu_9S_5 nanocrystals,[16] $Cu_{2−x}Se$ nanocrystals[20] and $W_{18}O_{49}$ untrathin nanowires[17] possess strong NIR absorption and high photothermal conversion efficiency, and can effectively kill cancer cells in vitro and in vivo.

Molybdenum oxide based materials, as important transition-metal oxides, are of significant importance for applications such as sensing,[27] catalysis,[28] energy storage.[29−31] Molybdenum oxides are especially interesting because some of their compounds with an oxygen deficiency, $MoO_{3−x}$, show an intense blue color,[32−35] imprecisely referred to as "molybdenum blues",[34,36] similar to the reported blue solution of copper chalcogenide nanocrystals with strong NIR absorption.[16,37,38] Recently, it is reported that the blue molybdenum oxide nanosheets display a large LSPR absorption peak, originating from the intervalence charge-transfer transition between Mo^V and Mo^{VI}.[33] Currently, the as-synthesized molybdenum oxide nanosheets or copper chalcogenide nanocrystals with NIR

absorption using oleylamine as a coordinating and reducing agent were coated with oleylamine molecules.[16,20,33,38] However, the long alkyl chains of oleylamine made them hydrophobic and less biocompatible. If these nanomaterials are employed for PTA therapy, complex post treatments such as ligand exchange or polymer/silica coating are needed to make them hydrophilic properties.[16,20,37,38] Therefore, these features trigger our interest to develop molybdenum oxide as a photothermal material.

Herein, we develop a simple method for synthesis of hydrophilic molybdenum oxide nanomaterials and investigate the influence of amount of surfactant and reaction temperature on the morphology, structure and LSPR properties of molybdenum oxide nanomaterials and further explore their potential in photothermal ablation of cancer cells.

■ EXPERIMENTAL SECTION

Materials. Molybdenum powder (99.5%), H_2O_2 (30 wt %) and poly(ethylene oxide) with a molar mass of 10 K Da (PEG) were purchased from Aladdin.

Preparation of Molybdenum Oxide Nanomaterials. The molybdenum precursor ($MoO_2(OH)(OOH)$) was prepared as follows.[34,35] 60 mL of H_2O_2 (30 wt %) aqueous solution was slowly added into a beaker containing 4.78 g of Mo powder (50 mmol) with magnetic stirring in an ice−water bath. Then a yellow solution was formed and continuously stirred to drive off excess H_2O_2. Subsequently, the solution was diluted to 100 mL to make the overall Mo concentration of 0.5 mol/L.

In a typical synthesis of molybdenum oxide nanospheres, 10 g of PEG was added to 20 mL of the above molybdenum precursor solution. Then the solution was magnetically stirred, forming a transparent yellow solution. Subsequently, the resulting solution was transferred to a poly(tetrafluoroethylene) (Teflon)-lined stainless steel autoclave (50 mL), which was sealed and treated at 90 °C for 12 h. A blue precipitate was collected by centrifugation and washed with water several times. For molybdenum oxide nanorods, 20 mL of the molybdenum precursor solution with no PEG additive was treated at 90 °C for 12 h. For molybdenum oxide nanoribbons, 10 g of PEG was added to 20 mL of the molybdenum precursor solution then treated at 150 °C for 12 h.

Measurement of Photothermal Performance. To measure the photothermal conversion performances of molybdenum oxide nanoribbons, radiation from a 980 nm laser was sent through a quartz cuvette containing an aqueous dispersion (0.3 mL) of the molybdenum oxide nanoribbons with different concentrations (i.e., 0, 1, 2, 4, 6, and 8 g/L). The 980 nm of semiconductor laser device (Xi'an Tours Radium Hirsh Laser Technology Co., Ltd., China) was independently calibrated to be an output power density of ~1 W/cm² using a handy optical power meter (Newport model 1918-C, CA, USA). A thermocouple with an accuracy of ±0.1 °C was inserted into the aqueous dispersion perpendicular to the path of the laser. The temperature was measured every 5 s.

Infrared Thermal Imaging and Photothermal Ablation of Cancer Cells in Vitro. Human osteosarcoma U2OS cells were maintained in Dulbecco's modified Eagle's medium (high glucose) (GIBCO, Invitrogen) and supplemented with 10% fetal bovine serum, 100 units/mL penicillin, and 100 mg/mL streptomycin in a humidified incubator under 5% CO_2 at 37 °C.

U2OS cells were seeded onto a 96-well plate at a density of 5×10^3 cells per well 1 day before the experiment. The cells were washed three times with PBS followed by incubation with culture medium containing molybdenum oxide nanoribbons (4 mg/mL) or PBS at 37 °C for 2 h. The cells were irradiated with a NIR laser (980 nm, 1 W/cm²) for 5 min or not. The infrared thermal imaging and temperatures from the labeled wells were detected by a photothermal therapy-monitoring system GX-A300 (Shanghai Guixin Corporation) with different time intervals during the laser irradiation. After laser irradiation, the cells were then treated with Hoechst 33258 (10 μg/

mL) for 1 h and stained with propidium iodide (PI, 100 μg/mL) for 30 min. The cells were washed with PBS three times and observed on Operetta high content analysis system (PerkinElmer). Meanwhile, the number of death cells in each well of the 96-well plate was counted by Operetta high content analysis system to quantitatively evaluate the effect of photothermal ablation after treatment. Three replicates were done for each treatment group.

Characterization. Sizes, morphologies, and microstructures of the samples were determined by a field emission scanning electron microscope (Hitachi S-4800) and field emission transmission electron microscope (JEOL, JEM-2100F). The elemental analysis of the sample was carried on the TEM equipped with an energy-dispersive X-ray spectroscopy (EDS). Powder X-ray diffraction (XRD) was conducted by a D/max-2550 PCX-ray diffractometer (Rigaku, Japan). UV-vis-NIR absorption spectra were measured on UV-vis 1901 Spectrophotometer (Phoenix). Fourier transform infrared (FTIR) spectra were recorded using the KBr pressed pellets on a RESTIGE-21 spectrometer (Shimadzu). Thermogravimetric analysis (TGA) measurements of the samples were done using the Discovery TGA instrument (TA Instruments, New Castle, DE, USA) under a nitrogen flow at the heating rate of 10 °C/min. Raman spectra were recorded on a Renishaw InVita Raman spectrometer with λ_{exc} = 633 nm. The sizes of nanomaterials were measured by random selection of 100 samples from the SEM or TEM images; then the mean values and standard deviations were calculated in statistics.

■ RESULTS AND DISCUSSION

In the present work, the molybdenum oxide nanomaterials prepared by a hydrothermal procedure, in which poly(ethylene glycol) (PEG, molecular weight, MW = 10 000 Da) as surfactant and reducing agent was added into the molybdenum precursor solution ($MoO_2(OH)(OOH)$)[35] to control the morphology of molybdenum oxide nanomaterials and endow their localized surface plasmon resonance (LSPR) property. This simplicity of the hydrothermal approach was compared favorably to a thermal decomposition of copper chalcogenide nanocrystals.[16,20] The impressive phenomenon was the color change of the final products. In the presence of PEG, the final products exhibited blue colors, ranging from light to very dark, depending on the amount of PEG and reaction temperature. While in the absence of PEG (e.g., 0 g), the molybdenum precursor solution kept its yellow color after 90 °C of hydrothermal treatment, and finally a white yellowish product was obtained, similar to the previous report.[34] From the low and high magnification of scanning electron microscopy (SEM) images (Figure 1a,b), the products contained nanorods with an average size of 23.9 ± 8.5 nm in diameter and 442.0 ± 88.9 nm in length. The triclinic monohydrate $MoO_3 \cdot H_2O$ (JCPDS card file no.: 26-1449) was the phase of main product identified by the XRD pattern, as shown in Figure 1c. However, the nanorods (0.2 mg/mL) showed negligible LSPR absorption in the near-infrared (NIR) region (Figure 1d), which was consistent with the white yellowish color (Figure 1d, inset) and thus not suitable as a photothermal materials derived by a NIR laser.

With PEG additive (e.g., 10 g), the as-obtained products exhibited dark blue after 90 °C of hydrothermal treatment of the yellow molybdenum precursor solution. As shown in the low magnification of a SEM image (Figure 2a), the blue products contained ball-like shapes of nanoparticles, and self-assembled and compactly piled up together forming wall structure, after drying a drop of concentrated aqueous solution on aluminum foil. From high magnification of a SEM image, the molybdenum oxide nanospheres exhibited varying sizes with an average diameter of 290.4 ± 66.7 nm (Figure 2b). To
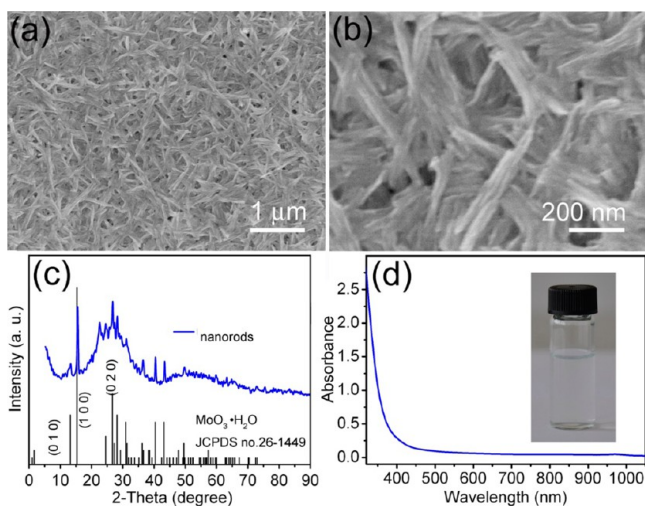
Figure 1. (a and b) Low and high magnification of SEM images; (c) XRD pattern; (d) UV−vis-NIR spectrum of molybdenum oxide nanorods prepared in the absence of PEG, inset showing a photograph of the aqueous dispersion.
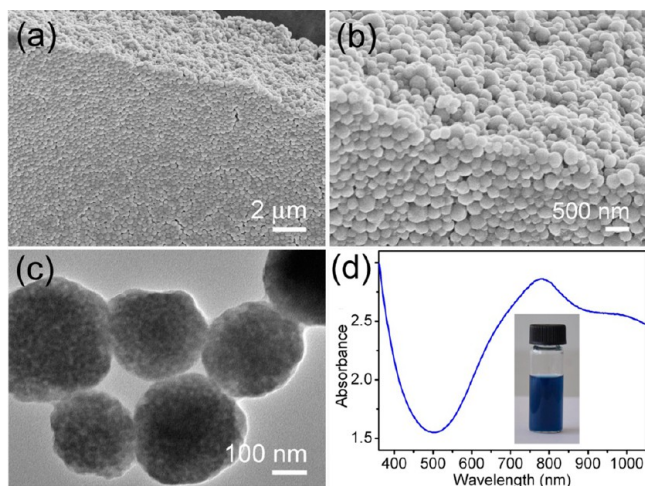

Figure 2. (a and b) Low and high magnification SEM images; (c) TEM image; (d) UV−vis-NIR spectrum of molybdenum oxide nanospheres prepared by 90 °C of hydrothermal treatment with 10 g of PEG additive, inset showing a photograph of the aqueous dispersion.

provide further insight into the structure, a transmission electron microscopy (TEM) image was recorded for the molybdenum oxide nanospheres, as shown in Figure 2c. These nanopsheres showed black alternating with white of the contrast, indicating their porous structure. After being repeatedly washed with ethanol enough times, this type of sample showed a partial redissolution, and low and high magnification of SEM images clearly indicated the sphere with polyhedral morphology (Figure S1a,b, Supporting Information), and the average diameter has become 262.2 ± 57.7 nm. TEM investigations showed that these nanospheres were assembled of smaller spheres-like units and mesoscale channels (Figure S1c, Supporting Information). Furthermore, high magnification of the TEM image showed that these smaller nanospheres contained mesoporous nanostructures and the mesochannels were arranged in a square lattice, with diameters of ~2.5 nm (Figure S1d, Supporting Information). TEM observation findings are consistent with the previous reported

results[35] and these mesoporous nanostructures are similar to that of mesoporous silica prepared by CTAB as soft template and thus have a potential as a nanocarrier for drug loading and delivering.[39,40] Besides their hierarchical porous structures, notably, the nanospheres (0.2 mg/mL) exhibited a stronger NIR absorption band from 500 to >1100 nm with an absorption peak at ~780 nm (Figure 2d), corresponding to their dark blue color (Figure 2d, inset), compared with the negligible absorption of molybdenum oxide nanorods (Figure 1d). This stronger NIR absorption endows the nanospheres a potential as NIR-laser-driven photothermal materials.

The energy-dispersive X-ray spectroscopy (EDS) result of the nanospheres (without extensive washing by ethanol) carried out in the TEM showed the presence of molybdenum, oxide and carbon (Figure S2 (Supporting Information), the Cu signal came from the copper grid substrate supporting the sample). However, the nanospheres exhibited very board peaks in the XRD pattern (Figure 3a, blue curve) and Raman spectrum
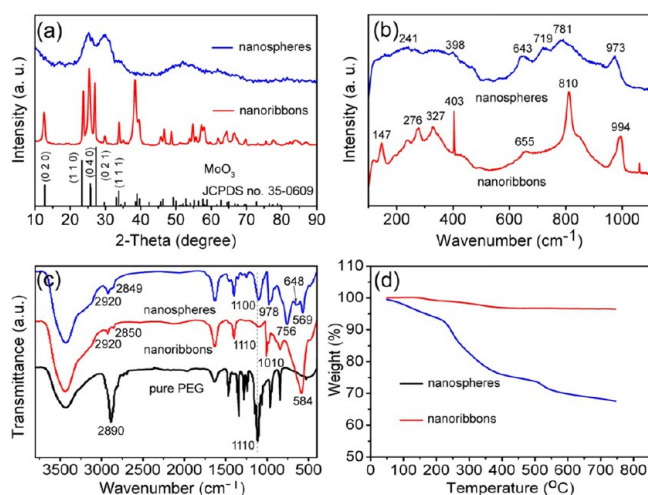

Figure 3. (a) XRD patterns; (b) Raman spectra; (c) FTIR spectra (black curve: pure PEG); (d) TGA spectra of molybdenum oxide nanospheres (blue curve), nanoribbons (red curve).

(Figure 3b, blue curve), indicating their poor crystal structure. Therefore, the structures of the as-obtained nanospheres were further characterized by the Fourier transform infrared (FTIR) spectra (Figure 3c, blue curve). The peak at 978 cm^{-1} is the characteristic of stretching vibrations of Mo=O. The sharp and broad peaks in the region 800−500 cm^{-1} (e.g., 756, 648, and 569 cm^{-1}) were attributed to stretching vibration of Mo—O— Mo.[41−43] The bands of 2920 and 2849 cm^{-1} were respectively assigned to the asymmetric and symmetric stretching vibrations of −CH$_2$− units in PEG chain.[44,45] The peak at 1100 cm^{-1} was corresponded to stretching vibration of C—O,[45] which was shifted ~10 cm^{-1} to lower wavenumber comparing to that of pure PEG (Figure 3c, black curve), probably due to the C—O of PEG coordinated with the molybdenum atoms.[17,46] Thermogravimetric analysis (TGA) (Figure 3d, blue curve) showed that the nanospheres suffered a weight loss of up to 25%, from 220 to 750 °C, indicating the presence of PEG in the sample, expected from the FTIR date. Considering the FTIR and TGA findings, the morphology changes of nanospheres after being extensively washed (Figure S1, Supporting Information) were probably due to the PEG partial redissolution. All these data indicate together that PEG was incorporated into the structure, creating porous hybrid

materials with features that were different from the polymer itself and conventional molybdenum oxide.[28,29,47] Besides, the intense blue color (Figure 2d, inset), as a characteristic of Mo^V or Mo^{IV},[33,34,47] indicated that partial Mo^{VI} was reduced to subvalent species due to the mild reducing of PEG, forming mixed-valence molybdenum oxide nanospheres.[34,35]

In the case of the surfactant-directing effect, the amount of the surfactant could strongly influence the reaction kinetics and thus determine the size and shape of the product.[48] Typically, at 90 °C and 2 g of PEG additive, morphological mixtures of rods and spheres were observed from the SEM image (Figure S3a, Supporting Information), partially due to the poor structure-directing ability of less amount of PEG molecules.[33] Whereas at the high concentration of PEG (e.g., 10, 15, or 20 g), a nanosphere-like morphology of molybdenum oxide was obtained, as shown in Figures 2a, S3b, and S3c (Supporting Information), respectively, due to the pseudo crown ether of PEG coordinated with the molybdenum atoms, blocking and freeing them, and thus controlling the growth kinetic of the nanoparticles.[34] Interestingly, all obtained blue nanospheres showed stronger LSPR absorption bands from 600 to 1100 nm (Figure S3d, Supporting Information), compared with that of molybdenum oxide nanorods (Figure 1d), Besides, the amount of PEG (e.g., 2−20 g) had no significant effect on the position of absorption band (Figure S3d, Supporting Information). However, these molybdenum oxide nanospheres exhibited very board peaks in the XRD pattern and more amounts of PEG (from 2 to 20 g) resulted in broader XRD peaks (blue curve of Figures 3a and S4 (Supporting Information)), indicating molybdenum oxide nanospheres with poor crystalline structures.

Molybdenum oxide nanoribbons were obtained by hydro-thermal treatment at 150 °C with 10 g of PEG additive. The low magnification of the SEM image represented a general view of the ribbon-like morphology and abundant nanoribbons lay and piled up together with average lengths of 766.8 ± 365.5 nm and widths of 117.8 ± 58.2 nm, as shown in Figure 4a. Interestingly, the nanoribbons were relatively transparent to the electron beam so that the lower ribbons could be observed
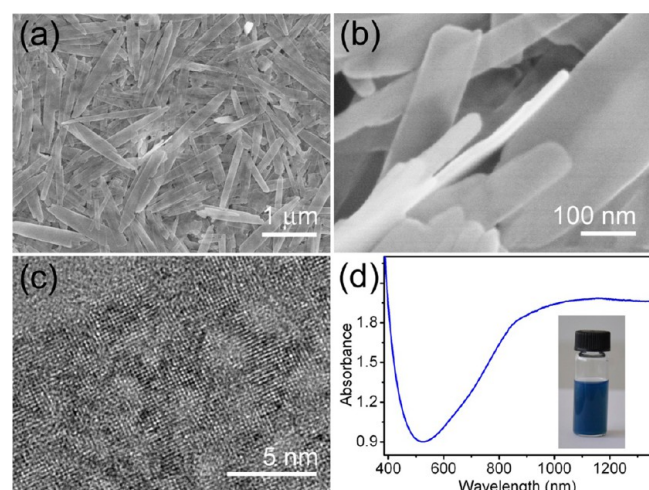
through the upper ones, indicating the nanoribbons were relatively thin. A careful examination from high magnification of the SEM image (Figure 4b) revealed that the nanoribbons were flat strips with a thickness of ~30 nm. To provide further insight into the structure, a high-resolution TEM (HRTEM) image showed clear lattice fringes, indicating a crystal structure (Figure 4c). Importantly, the nanoribbons exhibited a strong blue color (Figure 4d, inset) and showed an intense absorption band in the NIR region (Figure 4d). The nanoribbons (0.25 mg/mL) exhibited a minimum absorption around 520 nm and an increasing absorption with the increase of wavelength (520−1100 nm), similar to Cu$_{2-x}$S and WO$_{3-x}$.[16,17,26,37,38] Specially, the nanoribbons showed a broad absorption band starting from 1100 nm and extending to more than 1300 nm, probably due to their varying sizes. The absorption peak of nanoribbons in the NIR region underwent a red shift compared with that of molybdenum oxide nanospheres (Figure 2d). Importantly, this stronger absorption in NIR region (λ = 700−1100 nm) makes the nanoribbons a potential as 980 nm-laser-driven photo-thermal materials for ablation of cancer cells.

The XRD (Figure 3a, red curve) pattern and the Raman spectrum (Figure 3b, red curve) of the molybdenum oxide nanoribbons exhibited narrower and sharper peaks compared with those of nanospheres (Figure 3a,b, blue curve, respectively), indicating the higher crystalline structures of the nanoribbons. The XRD pattern (Figure 3a, red curve) could be matched to the orthorhombic MoO$_3$ (JCPDS card file no.: 35-0609) and also to orthorhombic H$_{0.34}$MoO$_3$ (JCPDS card file no.: 34-1230), which has diffraction patterns very close to orthorhombic MoO$_3$. In previous report, the blue samples of molybdenum oxide could also be indexed to hydrogen molybdenum bronzes (H$_x$MoO$_3$).[49] The Raman spectrum of the nanoribbons was shown in Figure 3b, red curve. Specifically, the peak at 994 cm^{-1} was assigned to the terminal oxygen (Mo=O) stretching mode of MoO$_3$,[47,50,51] and the peaks at 810 and 655 cm^{-1} were due to the stretching mode of doubly coordinated bridging oxygen (Mo$_2$−O) and the triply coordinated oxygen (Mo$_3$−O), respectively. However, the peaks of Mo$_2$−O and Mo$_3$−O stretching mode shifted ~10 cm^{-1} to lower wavenumbers compared with those of the literature at 821 and 666 cm^{-1}, respectively,[47,50,51] which was probably due to the modification of the original Mo$_2$−O and Mo$_3$−O bond by H$^+$ ions forming oxygen vacancies.[50] Meanwhile, the nanoribbons exhibited a blue color (Figure 4d, inset), uncharacteristic for pure MoO$_3$, indicating the presence of subvalent Mo^V or Mo^{IV} species.[33,34,47] Thus, partial Mo^{VI} was reduced to lower oxidation states within the nanoribbons by PEG, forming the slightly oxygen-deficient molybdenum oxide nanostructures, in accordance with the relatively broad XRD peaks. Notably, the LSPR of nanoribbons were probably originated from these oxygen-deficient structures. Therefore, the formula MoO$_{3-x}$ was proposed for the molybdenum oxide nanoribbons.

The FTIR spectrum of the nanoribbons (Figure 3c, red curve) showed that the peaks at 1010 and 584 cm^{-1} were attributed to the stretching vibration Mo=O and Mo—O—Mo of orthorhombic-MoO$_3$, respectively.[43,52] The bands of 2920 and 2850 cm^{-1} were assigned to the asymmetric and symmetric stretching vibrations of −CH$_2$− of the PEG chain,[44,45] respectively. The peak at ~1110 cm^{-1} corresponded to the stretching vibration of C—O,[44,45] in keeping with that of pure PEG (Figure 3c, black curve). From the TGA data (Figure 3d, red curve), it could be observed that the nanoribbons

Figure 4. (a and b) Low and high magnification of SEM images; (c) HRTEM image; (d) UV−vis−NIR spectrum of molybdenum oxide nanoribbons prepared by hydrothermal treatment at 150 °C with 10 g of PEG additive, inset showing a photograph of the aqueous dispersion.

3918

dx.doi.org/10.1021/am4050184 | ACS Appl. Mater. Interfaces 2014, 6, 3915−3922

showed a 2.6% weight loss from 200 to 700 °C, further confirming the presence of PEG on the nanoribbons.

It is known that crystallization at higher temperatures and pressures resulted in materials transforming to thermodynamically stable form.[34] Typically with 10 g of PEG additive, an increase of temperature from 90 to 150 °C (e.g., 105, 120, 135 and 150 °C) was a benefit for forming well-defined ribbon-like shapes and obtaining more ribbons and less spheres of morphology in the final products, as shown in Figure 5a,b,c
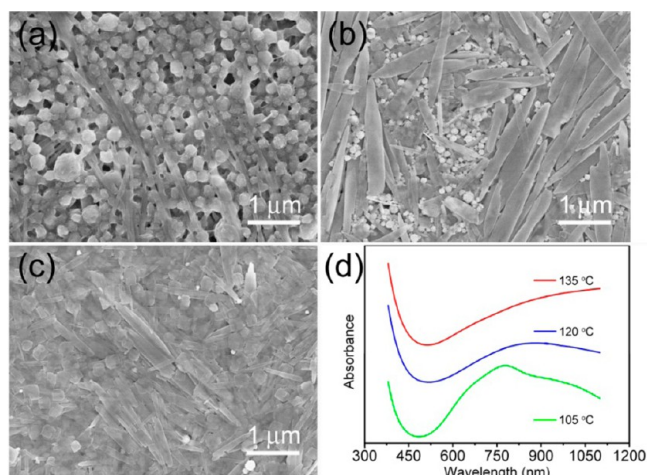

Figure 5. Molybdenum oxide nanomaterials prepared by hydrothermal treatment at different temperatures: (a) 105 °C, (b) 120 °C, and (c) 135 °C with 10 g of PEG additive. (d) UV−vis-NIR spectra of molybdenum oxide nanomaterials prepared by hydrothermal treatment at intermediate temperature: 135 °C (red curve), 120 °C (blue curve), and 105 °C (green curve) with 10 g of PEG additive.

and Figure 4a, respectively. At 105 °C, a MoO_3 (JCPDS card file no.: 35-0609) phase as the main product was formed (Figure S5, green curve, Supporting Information); at 120 °C, monoclinic MoO_2 (JCPDS card file no.: 65-5787) and MoO_3 (JCPDS card file no.: 35-0609) could be simutaneously obtained in the product (Figure S5, blue curve, Supporting Information), both corresponding with the mixture morphology of ribbons and spheres (Figure 5a,b). With further increases to 135 °C, the orthorhombic MoO_3 of the nanoribbons (JCPDS card file no.: 35-0609) became the main phase (Figure S5, red curve, Supporting Information). In

other words, with an increase of temperature, amorphous molybdenum oxide nanospheres first convert the mixture phase of MoO_2 and MoO_3 with the mixture morphology of flower-like crystalline nanospheres and nanoribbons, and then gradually transform to the thermodynamically stable orthorhombic phase of MoO_3 nanoribbons.[47]

The sample prepared at 105 °C showed a strong absorption band in the NIR region from 500 to 1100 nm and the absorption peak at ∼780 nm (Figure 5d, green curve), similar to that of the preparation at 90 °C. As the temperature is increased to 120 °C, the absorption peak underwent a red shift from 780 to 900 nm (Figure 5d, blue curve). Moreover, higher temperatures (e.g., 135 °C) further lead to the red shift of the absorption peak from 900 to >1100 nm (Figure 5d, red curve). Therefore, the LSPR absorption of the as-prepared molybdenum oxide nanomaterials can be regulated in certain range by adjusting the reaction temperature.

PEG was employed as a stabilizer of molybdenum oxide colloids to prevent their agglomeration and precipitation and further endowed them with a hydrophilic property. As a result, these molybdenum oxide nanomaterials could be readily dispersed in water with no complex post treatment such as ligands exchange or polymer/silica coating[16,37,38] and could thus be directly applied for biological applications.

The strong NIR absorption of molybdenum oxide nanomaterials motivated us to investigate their potential in photothermal ablation of cancer cells. Because the molybdenum oxide nanoribbons possess an increasing absorption with the increase of wavelength in the NIR region similar to $Cu_{2−x}S$ and $WO_{3−x}$,[16,17,26,37,38] herein, the nanoribbons were chosen as a model to explore their potential as a NIR laser-driven photothermal agent. Their photothermal conversion performance was examined in a quartz cuvette using the irradiation of a 980 nm laser with a power density of 1 W/cm², as shown in Figure S6 (Supporting Information). The temperature of the nanoribbon aqueous dispersions increased by 8.1 to 20.1 °C in 5 min, with the concentration increasing from 1 to 8 mg/mL. In contrast, the temperature of pure water (e.g., 0 mg/mL) increased by less than 3 °C from the initial temperature of 27 °C. Besides, after 5 min of irradiation (980 nm, 1 W/cm²), the NIR absorption of nanoribbons was retained relatively well, compared with that of no irradiation, as shown in the UV−vis-NIR spectrum of Figure S7 (Supporting Information). Therefore, molybdenum oxide nanoribbons could rapidly and
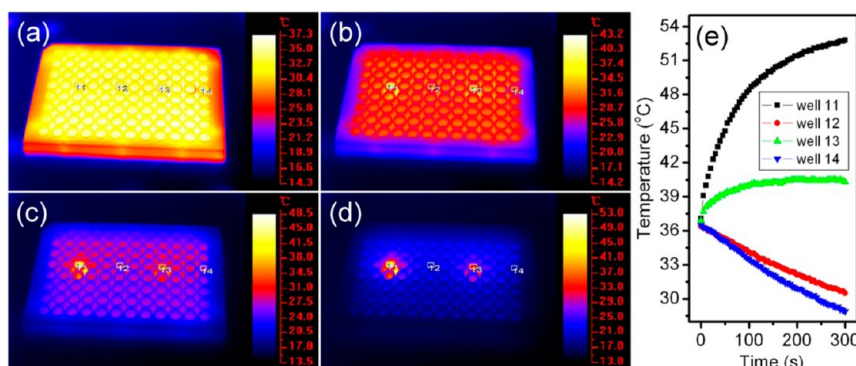

Figure 6. Infrared thermal imaging pictures of cancer cells treated with the $MoO_{3−x}$ + NIR group (well 11), $MoO_{3−x}$ control group (well 12), NIR control group (well 13), and PBS control group (well 14) cultured in 96-well plates captured at time points of (a) 0, (b) 30, (c) 90, and (d) 300 s under the laser irradiation (1 W/cm²) for 5 min. (e) Temperature profiles of the culture wells of 11−14 as a function of laser irradiated time. Note that the wells of 12 and 14 were used as controls without the laser exposure.

efficiently convert the NIR laser energy into heat and even have tolerance to the heat induced by laser illumination under the experiment conditions. These high photothermal conversion performance and photothernal stability is a prerequisite for efficient photothermal ablation of cancer cells.

Next, we explored the infrared thermal imaging and photothermal therapy in vitro using osteosarcoma U2OS cells incubated in a 96-well plate. These wells of cancer cells were divided into four groups (i.e., PBS control, NIR control, MoO_{3-x} control, and MoO_{3-x} + NIR, respectively). The cancer cells of PBS control and NIR control group were cultured with medium containing PBS, whereas the cancer cells of MoO_{3-x} control and MoO_{3-x} + NIR group were cultured with containing molybdenum oxide nanoribbons (MoO_{3-x}, 4 mg/mL). After 2 h, the cancer cells of the NIR control and MoO_{3-x} + NIR group were then irradiated by two 980 nm lasers (1 W/cm^2) for 5 min, simultaneously. The PBS control and MoO_{3-x} control group received no irradiation. Three replicates were done for each treatment group. The infrared thermal imaging and temperatures from the labeled wells were detected with different time intervals during the laser irradiation, as shown in Figure 6. Following laser irradiation, these cancer cells were double stained with Hoechst 33258 and propidium iodide (PI), and then observed on an operetta high content analysis system (PerkinElmer). Bright field images show the morphology of corresponding cancer cells, Hoechst 33258 stained cells represent the total cells of the well (blue color, indicating nucleus), and PI stained cells represent dead cells (red color), as shown in Figure 7a. Meanwhile, the number of death cells in each group was also counted by Operetta high content analysis system to quantitatively evaluate the effect of photothermal treatment, as shown in Figure 7b.

Infrared thermal imaging pictures of MoO_{3-x} + NIR (well 11), MoO_{3-x} control (well 12), NIR control (well 13), and PBS control (well 14) with different time intervals are shown in Figure 6. The well 11 of MoO_{3-x} + NIR showed a yellow color and became brighter and larger, whereas the well 13 of the NIR control was still a little red under the same irradiation condition for 5 min. As expected, the nanoribbons exhibit a high contrast for infrared thermal imaging (Figure 6a−d). Notably, the obvious temperature elevation and efficient photothermal ablation of the cancer cells were observed only after laser irradiation in the presence of the nanoribbons (Figures 6e and 7). For the NIR control group, only 3.4 °C of an increase was observed (Figure 6e) and 5 min of irradiation induced no increasing cell death (1.47%), compared with the control group (1.32%), as shown in Figure 7. That is because the low heat energy converted from the 980 nm laser by cultured medium was not enough to kill the cancer cells. Meanwhile, in the case of the MoO_{3-x} control group, no obvious cell death was observed (1.30%, Figure 7). In contrast, for the MoO_{3-x} + NIR group, the temperature was increased very quickly and reached up to 53.0 from 37.3 °C (Figure 6e), and the majority of cancer cells (81.27%) were killed (Figure 7) after 5 min of the irradiation. On the basis of the fact that the laser irradiation did not cause any acute damage to cancer cells and no obvious cell death happened in the nanoribbons, incubated cells without irradiation, and only the wells containing the nanoribbons with irradiation show high contrast in infrared thermal images and effective ablation of cancer cells, we attribute the above treatment effect to the high photothermal conversion ability of the nanoribbons. This evidence demonstrated the molybdenum
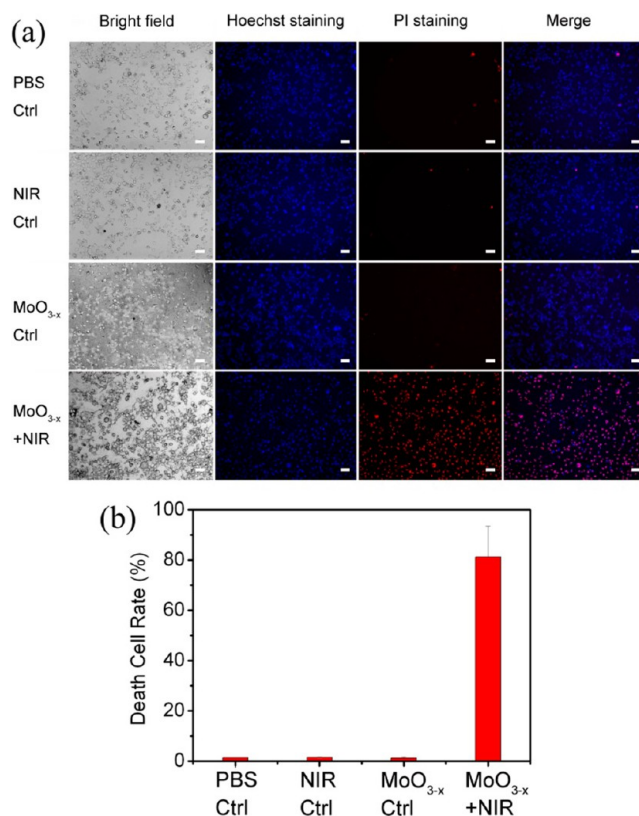

Figure 7. (a) Fluorescence microscopy images of cancer cells treated with PBS control, NIR control, MoO_{3-x} control and MoO_{3-x} + NIR, then stained with Hoechst 33258, propidium iodide (PI) before observing on Operetta high content analysis system (PerkinElmer). The bright field image shows the morphology of corresponding cancer cells, Hoechst 33258 stained cells (blue color, indicating nucleus) represent the total cells of the well, and PI stained cells (red color) represent dead cells. Scale bar equals 100 μm; (b) death cells rates in each group analyzed by Operetta high content analysis system to quantitatively evaluate the effect of photothermal treatment. Error bars were based on the standard deviations of three parallel experiments. Herein, molybdenum oxide nanoribbons were abbreviated as MoO_{3-x}.

oxide nanoribbons as a promising photothermal conversion candidate for cancer treatments.

■ CONCLUSION

In summary, we have developed a simple hydrothermal route for hydrophilic molybdenum oxide nanospheres and nanoribbons with strong LSPR absorption in the NIR region. The presence of PEG plays two important roles in the formation of molybdenum oxide nanomaterials: (1) acting as a mild reducing agent of Mo^{VI} to subvalent species to make them with certain oxygen deficiencies, thus as-prepared molybdenum oxide materials possess LSPR absorption and (2) acting as stabilizers of molybdenum oxide to prevent agglomeration and precipitation, making them hydrophilic. Importantly, the evolution of molybdenum oxide nanospheres to nanoribbons and red shift of LSPR absorption could be realized by increasing the reaction temperature. More importantly, these nanoribbons can efficiently convert the 980 nm laser energy into heat energy and effectively kill cancer cells by thermal ablation. In the future, systematical toxicity examination, photothermal therapy in vivo, and synergistic effects combining with targeting, chemotherapy or radiotherapy may be studied in order to develop better therapeutic agents. Even so, our

preliminary results shed light on a potential of molybdenum oxide based nanomaterials as a novel, low cost, and effective photothermal material.

■ ASSOCIATED CONTENT

Ⓢ Supporting Information

SEM, TEM, and EDS of molybdenum oxide nanospheres; SEM images and XRD of molybdenum oxide nanomaterials prepared by hydrothermal treatment at 90 °C with different amounts of PEG; XRD patterns of molybdenum oxide nanomaterials as prepared by hydrothermal treatment at intermediate temperature; temperature elevation of molybdenum oxide nanoribbons and UV−vis-NIR spectrum of molybdenum oxide nanoribbons before and after NIR irradiation; death cells rates of osteoblast normal cells in each group; TEM of osteosarcoma U2OS cells cultured with molybdenum oxide nanomaterials. This material is available free of charge via the Internet at http://pubs.acs.org.

■ AUTHOR INFORMATION

Corresponding Authors
*R. Hu. E-mail: coryhu@sibs.ac.cn.
*R. Zou. E-mail: rjzou@dhu.edu.cn.
*J. Hu. E-mail: hu.junqing@dhu.edu.cn.

Author Contributions
§These authors contributed equally to this work.

Notes
The authors declare no competing financial interest.

■ ACKNOWLEDGMENTS

■ REFERENCES

(1) Gong, H.; Cheng, L.; Xiang, J.; Xu, H.; Feng, L.; Shi, X.; Liu, Z. Near-Infrared Absorbing Polymeric Nanoparticles as a Versatile Drug Carrier for Cancer Combination Therapy. *Adv. Funct. Mater.* **2013**, *23*, 6059−6067.

(2) Wang, C.; Xu, H.; Liang, C.; Liu, Y.; Li, Z.; Yang, G.; Cheng, H.; Li, Y.; Liu, Z. Iron Oxide @ Polypyrrole Nanoparticles as a Multifunctional Drug Carrier for Remotely Controlled Cancer Therapy with Synergistic Antitumor Effect. *ACS Nano* **2013**, *7*, 6782−6795.

(3) Liu, Y.; Ai, K.; Liu, J.; Deng, M.; He, Y.; Lu, L. Dopamine-Melanin Colloidal Nanospheres: an Efficient Near-Infrared Photothermal Therapeutic Agent for in Vivo Cancer Therapy. *Adv. Mater.* **2013**, *25*, 1353−1359.

(4) Chou, S. S.; Kaehr, B.; Kim, J.; Foley, B. M.; De, M.; Hopkins, P. E.; Huang, J.; Brinker, C. J.; Dravid, V. P. Chemically Exfoliated MoS₂ as Near-Infrared Photothermal Agents. *Angew. Chem., Int. Ed.* **2013**, *125*, 4254−4258.

(5) Zha, Z.; Yue, X.; Ren, Q.; Dai, Z. Uniform Polypyrrole Nanoparticles with High Photothermal Conversion Efficiency for Photothermal Ablation of Cancer Cells. *Adv. Mater.* **2013**, *25*, 777−782.

(6) Zhang, Z.; Wang, L.; Wang, J.; Jiang, X.; Li, X.; Hu, Z.; Ji, Y.; Wu, X.; Chen, C. Mesoporous Silica-Coated Gold Nanorods as a Light-Mediated Multifunctional Theranostic Platform for Cancer Treatment. *Adv. Mater.* **2012**, *24*, 1418−1423.

(7) Jang, B.; Park, J. Y.; Tung, C. H.; Kim, I. H.; Choi, Y. Gold Nanorod-Photosensitizer Complex for Near-Infrared Fluorescence Imaging and Photodynamic/Photothermal Therapy In Vivo. *ACS Nano* **2011**, *5*, 1086−1094.

(8) Huang, X. Q.; Tang, S. H.; Mu, X. L.; Dai, Y.; Chen, G. X.; Zhou, Z. Y.; Ruan, F. X.; Yang, Z. L.; Zheng, N. F. Freestanding Palladium Nanosheets with Plasmonic and Catalytic Properties. *Nat. Nanotechnol.* **2011**, *6*, 28−32.

(9) Dickerson, E. B.; Dreaden, E. C.; Huang, X. H.; El-Sayed, I. H.; Chu, H. H.; Pushpanketh, S.; McDonald, J. F.; El-Sayed, M. A. Gold Nanorod Assisted Near-Infrared Plasmonic Photothermal Therapy (PPTT) of Squamous Cell Carcinoma in Mice. *Cancer Lett.* **2008**, *269*, 57−66.

(10) Alkilany, A. M.; Thompson, L. B.; Boulos, S. P.; Sisco, P. N.; Murphy, C. J. Gold Nanorods: Their Potential for Photothermal Therapeutics and Drug Delivery, Tempered by the Complexity of Their Biological Interactions. *Adv. Drug Delivery Rev.* **2012**, *64*, 190−199.

(11) Xia, Y.; Li, W.; Cobley, C. M.; Chen, J.; Xia, X.; Zhang, Q.; Yang, M.; Cho, E. C.; Brown, P. K. Gold Nanocages: From Synthesis to Theranostic Applications. *Acc. Chem. Res.* **2011**, *44*, 914−924.

(12) Liu, H.; Liu, T.; Wu, X.; Li, L.; Tan, L.; Chen, D.; Tang, F. Targeting Gold Nanoshells on Silica Nanorattles: a Drug Cocktail to Fight Breast Tumors via a Single Irradiation with Near-Infrared Laser Light. *Adv. Mater.* **2012**, *24*, 755−761.

(13) Liu, H.; Chen, D.; Li, L.; Liu, T.; Tan, L.; Wu, X.; Tang, F. Multifunctional Gold Nanoshells on Silica Nanorattles: A Platform for the Combination of Photothermal Therapy and Chemotherapy with Low Systemic Toxicity. *Angew. Chem., Int. Ed.* **2011**, *50*, 891−895.

(14) Fang, W.; Yang, J.; Gong, J.; Zheng, N. Photo- and pH-Triggered Release of Anticancer Drugs from Mesoporous Silica-Coated Pd@Ag Nanoparticles. *Adv. Funct. Mater.* **2012**, *22*, 842−848.

(15) Lal, S.; Clare, S. E.; Halas, N. J. Nanoshell-Enabled Photothermal Cancer Therapy: Impending Clinical Impact. *Acc. Chem. Res.* **2008**, *41*, 1842−1851.

(16) Tian, Q.; Jiang, F.; Zou, R.; Liu, Q.; Chen, Z.; Zhu, M.; Yang, S.; Wang, J.; Wang, J.; Hu, J. Hydrophilic Cu₉S₅ Nanocrystals: A Photothermal Agent with a 25.7% Heat Conversion Efficiency for Photothermal Ablation of Cancer Cells in Vivo. *ACS Nano* **2011**, *5*, 9761−9771.

(17) Chen, Z.; Wang, Q.; Wang, H.; Zhang, L.; Song, G.; Song, L.; Hu, J.; Wang, H.; Liu, J.; Zhu, M.; Zhao, D. Ultrathin PEGylated W₁₈O₄₉ Nanowires as a New 980 nm-Laser-Driven Photothermal Agent for Efficient Ablation of Cancer Cells in Vivo. *Adv. Mater.* **2013**, *25*, 2095−2100.

(18) Kriegel, I.; Jiang, C.; Rodriguez-Fernandez, J.; Schaller, R. D.; Talapin, D. V.; da Como, E.; Feldmann, J. Tuning the Excitonic and Plasmonic Properties of Copper Chalcogenide Nanocrystals. *J. Am. Chem. Soc.* **2012**, *134*, 1583−1590.

(19) Hsu, S.-W.; On, K.; Tao, A. R. Localized Surface Plasmon Resonances of Anisotropic Semiconductor Nanocrystals. *J. Am. Chem. Soc.* **2011**, *133*, 19072−19075.

(20) Hessel, C. M.; Pattani, V. P.; Rasch, M.; Panthani, M. G.; Koo, B.; Tunnell, J. W.; Korgel, B. A. Copper Selenide Nanocrystals for Photothermal Therapy. *Nano Lett.* **2011**, *11*, 2560−2566.

(21) Dorfs, D.; Härtling, T.; Miszta, K.; Bigall, N. C.; Kim, M. R.; Genovese, A.; Falqui, A.; Povia, M.; Manna, L. Reversible Tunability of the Near-Infrared Valence Band Plasmon Resonance in Cu₂₋ₓSe Nanocrystals. *J. Am. Chem. Soc.* **2011**, *133*, 11175−11180.

(22) Li, W.; Zamani, R.; Rivera Gil, P.; Pelaz, B.; Ibáñez, M.; Cadavid, D.; Shavel, A.; Alvarez-Puebla, R. A.; Parak, W. J.; Arbiol, J.; Cabot, A.

CuTe Nanocrystals: Shape and Size Control, Plasmonic Properties, and Use as SERS Probes and Photothermal Agents. *J. Am. Chem. Soc.* **2013**, *135*, 7098−7101.

(23) Manthiram, K.; Alivisatos, A. P. Tunable Localized Surface Plasmon Resonances in Tungsten Oxide Nanocrystals. *J. Am. Chem. Soc.* **2012**, *134*, 3995−3998.

(24) Garcia, G.; Buonsanti, R.; Runnerstrom, E. L.; Mendelsberg, R. J.; Llordes, A.; Anders, A.; Richardson, T. J.; Milliron, D. J. Dynamically Modulating the Surface Plasmon Resonance of Doped Semiconductor Nanocrystals. *Nano Lett.* **2011**, *11*, 4415−4420.

(25) Buonsanti, R.; Llordes, A.; Aloni, S.; Helms, B. A.; Milliron, D. J. Tunable Infrared Absorption and Visible Transparency of Colloidal Aluminum-Doped Zinc Oxide Nanocrystals. *Nano Lett.* **2011**, *11*, 4706−4710.

(26) Tian, Q.; Tang, M.; Sun, Y.; Zou, R.; Chen, Z.; Zhu, M.; Yang, S.; Wang, J.; Wang, J.; Hu, J. Hydrophilic Flower-Like CuS Superstructures as an Efficient 980 nm Laser-Driven Photothermal Agent for Ablation of Cancer Cells. *Adv. Mater.* **2011**, *23*, 3542−3547.

(27) Ouyang, Q.-Y.; Li, L.; Wang, Q.-S.; Zhang, Y.; Wang, T.-S.; Meng, F.-N.; Chen, Y.-J.; Gao, P. Facile synthesis and enhanced H_2S sensing performances of Fe-doped α-MoO_3 micro-structures. *Sens. Actuators, B* **2012**, *169*, 17−25.

(28) Pan, W.; Tian, R.; Jin, H.; Guo, Y.; Zhang, L.; Wu, X.; Zhang, L.; Han, Z.; Liu, G.; Li, J.; Rao, G.; Wang, H.; Chu, W. Structure, Optical, and Catalytic Properties of Novel Hexagonal Metastable h-MoO_3 Nano- and Microrods Synthesized with Modified Liquid-Phase Processes. *Chem. Mater.* **2010**, *22*, 6202−6208.

(29) Liang, R.; Cao, H.; Qian, D. MoO_3 Nanowires as Electrochemical Pseudocapacitor Materials. *Chem. Commun.* **2011**, *47*, 10305−10307.

(30) Shi, Y.; Guo, B.; Corr, S. A.; Shi, Q.; Hu, Y.-S.; Heier, K. R.; Chen, L.; Seshadri, R.; Stucky, G. D. Ordered Mesoporous Metallic MoO_2 Materials with Highly Reversible Lithium Storage Capacity. *Nano Lett.* **2009**, *9*, 4215−4220.

(31) Jasieniak, J. J.; Seifter, J.; Jo, J.; Mates, T.; Heeger, A. J. A Solution-Processed MoO_x Anode Interlayer for Use within Organic Photovoltaic Devices. *Adv. Funct. Mater.* **2012**, *22*, 2594−2605.

(32) Greenblatt, M. Molybdenum Oxide Bronzes with Quasi-Low-Dimensional Properties. *Chem. Rev.* **1988**, *88*, 31−53.

(33) Huang, Q.; Hu, S.; Zhuang, J.; Wang, X. $MoO_{(3−x)}$-Based Hybrids with Tunable Localized Surface Plasmon Resonances: Chemical Oxidation Driving Transformation from Ultrathin Nanosheets to Nanotubes. *Chem.—Eur. J.* **2012**, *18*, 15283−15287.

(34) Munoz-Espi, R.; Burger, C.; Krishnan, C. V.; Chu, B. Polymer-Controlled Crystallization of Molybdenum Oxides from Peroxomolybdates: Structural Diversity and Application to Catalytic Epoxidation. *Chem. Mater.* **2008**, *20*, 7301−7311.

(35) Chen, J. L.; Burger, C.; Krishnan, C. V.; Chu, B. Morphogenesis of Highly Ordered Mixed-Valent Mesoporous Molybdenum Oxides. *J. Am. Chem. Soc.* **2005**, *127*, 14140−14141.

(36) Muller, A.; Serain, C. Soluble Molybdenum Blues - "des pudels kern". *Acc. Chem. Res.* **2000**, *33*, 2−10.

(37) Song, G.; Wang, Q.; Wang, Y.; Lv, G.; Li, C.; Zou, R.; Chen, Z.; Qin, Z.; Huo, K.; Hu, R.; Hu, J. A Low-Toxic Multifunctional Nanoplatform Based on Cu_9S_5@$mSiO_2$ Core-Shell Nanocomposites: Combining Photothermal- and Chemotherapies with Infrared Thermal Imaging for Cancer Treatment. *Adv. Funct. Mater.* **2013**, *23*, 4281−4292.

(38) Tian, Q.; Hu, J.; Zhu, Y.; Zou, R.; Chen, Z.; Yang, S.; Li, R.; Su, Q.; Han, Y.; Liu, X. Sub-10 nm Fe_3O_4@$Cu_{2−x}S$ Core-Shell Nanoparticles for Dual-Modal Imaging and Photothermal Therapy. *J. Am. Chem. Soc.* **2013**, *135*, 8571−8577.

(39) Song, G.; Li, C.; Hu, J.; Zou, R.; Xu, K.; Han, L.; Wang, Q.; Yang, J.; Chen, Z.; Qin, Z.; Ruan, K.; Hu, R. A Simple Transformation from Silica Core-Shell-Shell to Yolk-Shell Nanostructures: a Useful Platform for Effective Cell Imaging and Drug Delivery. *J. Mater. Chem.* **2012**, *22*, 17011−17018.

(40) Han, L.; Zhou, Y.; He, T.; Song, G.; Wu, F.; Jiang, F.; Hu, J. One-Pot Morphology-Controlled Synthesis of Various Shaped Mesoporous Silica Nanoparticles. *J. Mater. Sci.* **2013**, *48*, 5718−5726.

(41) Han, W.; Yuan, P.; Fan, Y.; Liu, H.; Bao, X. Synthesis, Self-Assembly and Disassembly of Mono-Dispersed Mo-Based Inorganic-Organic Hybrid Nanocrystals. *J. Mater. Chem.* **2012**, *22*, 12121−12127.

(42) Fang, L.; Shu, Y. Y.; Wang, A. Q.; Zhang, T. Green Synthesis and Characterization of Anisotropic Uniform Single-Crystal Alpha-MoO_3 Nanostructures. *J. Phys. Chem. C* **2007**, *111*, 2401−2408.

(43) Chithambararaj, A.; Bose, A. C. Hydrothermal Synthesis of Hexagonal and Orthorhombic MoO_3 Nanoparticles. *J. Alloys Compd.* **2011**, *509*, 8105−8110.

(44) Wang, H.; Peng, M.; Zheng, J.; Li, P. Encapsulation of Silica Nanoparticles by Redox-Initiated Graft Polymerization from the Surface of Silica Nanoparticles. *J. Colloid Interface Sci.* **2008**, *326*, 151−157.

(45) Cauda, V.; Argyo, C.; Bein, T. Impact of Different PEGylation Patterns on the Long-Term Bio-Stability of Colloidal Mesoporous Silica Nanoparticles. *J. Mater. Chem.* **2010**, *20*, 8693−8699.

(46) Xu, Y.; Chen, D.; Jiao, X.; Xue, K. Nanosized Cu_2O/PEG400 Composite Hollow Spheres with Mesoporous Shells. *J. Phys. Chem. C* **2007**, *111*, 16284−16289.

(47) Krishnan, C. V.; Chen, J. L.; Burger, C.; Chu, B. Polymer-Assisted Growth of Molybdenum Oxide Whiskers via a Sonochemical Process. *J. Phys. Chem. B* **2006**, *110*, 20182−20188.

(48) Koziej, D.; Rossell, M. D.; Ludi, B.; Hintennach, A.; Novak, P.; Grunwaldt, J.-D.; Niederberger, M. Interplay Between Size and Crystal Structure of Molybdenum Dioxide Nanoparticles-Synthesis, Growth Mechanism, and Electrochemical Performance. *Small* **2011**, *7*, 377−387.

(49) Hu, X. K.; Qian, Y. T.; Song, Z. T.; Huang, J. R.; Cao, R.; Xiao, J. Q. Comparative Study on MoO_3 and H_xMoO_3 Nanobelts: Structure and Electric Transport. *Chem. Mater.* **2008**, *20*, 1527−1533.

(50) Ou, J. Z.; Campbell, J. L.; Yao, D.; Wlodarski, W.; Kalantar-zadeh, K. In Situ Raman Spectroscopy of H_2 Gas Interaction with Layered MoO_3. *J. Phys. Chem. C* **2011**, *115*, 10757−10763.

(51) Rajagopal, S.; Nataraj, D.; Khyzhun, O. Y.; Djaoued, Y.; Robichaud, J.; Senthil, K.; Mangalaraj, D. Systematic Synthesis and Analysis of Change in Morphology, Electronic Structure and Photoluminescence Properties of Pyrazine Intercalated MoO_3 Hybrid Nanostructures. *CrystEngComm* **2011**, *13*, 2358−2368.

(52) Wang, S.; Gao, Q.; Zhang, Y.; Gao, J.; Sun, X.; Tang, Y. Controllable Synthesis of Organic-Inorganic Hybrid MoO_x/Polyaniline Nanowires and Nanotubes. *Chem.—Eur. J.* **2011**, *17*, 1465−1472.